Title: Functional quantitative susceptibility mapping (fQSM)

Article Type: Regular Article

Corresponding Author: Dr. Dávid Z Balla, Dr. rer. nat.

Corresponding Author's Institution: Max Planck Institute for Biological Cybernetics

First Author: Dávid Z Balla, Dr. rer. nat.

Order of Authors: Dávid Z Balla, Dr. rer. nat.; Rosa M Sanchez-Panchuelo, PhD; Samuel J Wharton, PhD; Gisela E Hagberg, Dr.; Klaus Scheffler, Dr.; Susan T Francis, PhD; Richard Bowtell, PhD

Abstract: Blood oxygenation level dependent (BOLD) functional magnetic resonance imaging (fMRI) is a powerful technique, typically based on the statistical analysis of the magnitude component of the complex time-series. Here, we additionally interrogated the phase data of the fMRI time-series and used quantitative susceptibility mapping (QSM) in order to investigate the potential of functional QSM (fQSM) relative to standard magnitude BOLD fMRI. High spatial resolution data (1 mm isotropic) were acquired every 3 seconds using zoomed multi-slice gradient-echo EPI collected at 7 T in single orientation (SO) and multiple orientation (MO) experiments, the latter involving 4 repetitions with the subject's head rotated relative to B0. Statistical parametric maps (SPM) were reconstructed for magnitude, phase and QSM time-series and each was subjected to detailed analysis. Several fQSM pipelines were evaluated and compared based on the relative number of voxels that were coincidentally found to be significant in QSM and magnitude SPMs (common voxels). We found that sensitivity and spatial reliability of fQSM relative to the magnitude data depended strongly on the arbitrary significance threshold defining "activated" voxels in SPMs, and on the efficiency of spatio-temporal filtering of the phase time-series. Sensitivity and spatial reliability depended slightly on whether MO or SO fQSM was performed and on the QSM calculation approach used for SO data. Our results present the potential of fQSM as a quantitative method of mapping BOLD changes. We also critically discuss the technical challenges and issues linked to this intriguing new technique.

Functional quantitative susceptibility mapping (fQSM)

Dávid Z. Balla [a,b], Rosa M. Sanchez-Panchuelo [b], Samuel J. Wharton [b], Gisela E. Hagberg [a,c], Klaus Scheffler [a,c], Susan T. Francis [b], and Richard Bowtell [b]

[a] High-Field MR Centre, Max-Planck-Institute for Biological Cybernetics, Tübingen, Germany

[b] Sir Peter Mansfield Magnetic Resonance Centre, School of Physics and Astronomy, University of Nottingham, Nottingham, United Kingdom

[c] Department for Biomedical Magnetic Resonances, University of Tübingen, Tübingen, Germany

Corresponding author: Dávid Z. Balla

Spemannstr. 41

72076 Tübingen

Germany

Tel.: +49-7071-601724

Fax: +49-7071-601702

Email: david.balla@tuebingen.mpg.de

Abstract

Blood oxygenation level dependent (BOLD) functional magnetic resonance imaging (fMRI) is a powerful technique, typically based on the statistical analysis of the magnitude component of the complex time-series. Here, we additionally interrogated the phase data of the fMRI time-series and used quantitative susceptibility mapping (QSM) in order to investigate the potential of functional QSM (fQSM) relative to standard magnitude BOLD fMRI. High spatial resolution data (1 mm isotropic) were acquired every 3 seconds using zoomed multi-slice gradient-echo EPI collected at 7 T in single orientation (SO) and multiple orientation (MO) experiments, the latter involving 4 repetitions with the subject's head rotated relative to B_0. Statistical parametric maps (SPM) were reconstructed for magnitude, phase and QSM time-series and each was subjected to detailed analysis. Several fQSM pipelines were evaluated and compared based on the relative number of voxels that were coincidentally found to be significant in QSM and magnitude SPMs (common voxels). We found that sensitivity and spatial reliability of fQSM relative to the magnitude data depended strongly on the arbitrary significance threshold defining "activated" voxels in SPMs, and on the efficiency of spatio-temporal filtering of the phase time-series. Sensitivity and spatial reliability depended slightly on whether MO or SO fQSM was performed and on the QSM calculation approach used for SO data. Our results present the potential of fQSM as a quantitative method of mapping BOLD changes. We also critically discuss the technical challenges and issues linked to this intriguing new technique.

Keywords: fMRI; functional QSM; MR phase imaging; susceptibility mapping; quantitative BOLD; specific brain activation.

Abbreviations: AP, anterior-posterior; COSMOS, calculation of susceptibility through multiple orientation sampling; DORK, dynamic off-resonance correction in k-space; FWHM, full-width at half maximum; HF, head-foot; HRF, hemodynamic response function; MC, motion correction; MO, multiple orientation; MRAD, milliradian; NVR, nuisance variable regression; PPB, parts per billion; QSM, quantitative susceptibility mapping; RELPOLY, relative polynomial filtering; RETROICOR, image-based retrospective correction of physiological motion effects; RL, right-left; RSO, regularized single orientation algorithm; SENSE, sensitivity encoding; SHARP, sophisticated harmonic artifact reduction for phase data; SI, superior-inferior; SO, single orientation dataset; TKD, thresholded k-space division algorithm.

1. Introduction

Functional MRI (fMRI) based on the BOLD-effect is widely used as a non-invasive tool for mapping brain activity (Kim and Ogawa, 2012). The increase in the BOLD contrast-to-noise ratio (CNR) with magnetic field strength has provided one of the main motivations for the technical development of MRI systems operating at ever higher magnetic field strength (Uğurbil, 2012). Nevertheless, the BOLD-effect is a secondary product of neural activation, relying on changes in blood flow which depend upon the coupling of the brain's vasculature to neuronal activation. Hence the neural specificity of the BOLD effect is physiologically limited by the brain's hemodynamics (Logothetis, 2008). Downstream spreading of the changes in blood oxygenation from the capillary bed at the activation site to distal veins draining blood from a larger brain volume areas exacerbates this intrinsic loss of specificity (Turner, 2002). Besides this loss of neural specificity, there is an additional loss of vascular specificity due to partial voluming effects arising from both the intrinsic spatial resolution (signal sampling) and the spatial extent of the field perturbations produced by vascular structures. Partial voluming effects due to limited spatial sampling can be reduced by investing the higher CNR of high magnetic field in improving the spatial resolution. Non-local magnetic field perturbation effects are caused by the microscopic local changes of the susceptibility of blood and the spatial extent of magnetic field perturbations due to veins is larger than that due to capillaries. Since the field perturbation is a function of susceptibility (depending directly on blood oxygenation) and field strength, BOLD magnetic field perturbations from the same source increase with field strength.

Conventionally, BOLD-contrast is measured from the magnitude image time-series, where the non-local intensity changes related to susceptibility changes are less pronounced than in phase time-series. Only a few studies have investigated BOLD contrast by also using the phase information in time-series (Arja et al., 2010; Bianciardi et al., 2013; Chen et al., 2013; Hagberg et al., 2008; Hagberg et al., 2012; Hahn et al., 2009; Menon, 2002; Petridou et al., 2009; Rowe, 2005; Rowe and Logan, 2004; Rowe et al., 2007; Tomasi and Caparelli, 2007). At the spatial resolution allowed by conventional magnetic fields (e.g. 1.5 T and 3 T), the BOLD phase effect, despite being stronger than the magnitude effect at microscopic level, is averaged out due to the orientation dependence of microscopic field perturbation effects, hence substantial phase contrast can only be found near a few large veins of diameter comparable to the voxel dimensions. At high spatial resolution, the phase of the fMRI time-series has been used to identify the dominant non-local BOLD effects due to large veins and to remove their contribution from the conventional magnitude BOLD statistical maps (Menon, 2002). Recently, a novel biophysical model for phase changes in BOLD fMRI based on the Lorentz-sphere approach was proposed (Zhao et al., 2007). This predicts that a non-zero average phase change occurs in the parenchyma due to BOLD effects in the vasculature (Feng et al., 2009). Experimental validation of the predicted maximum BOLD phase contrast of 17 mrad was performed by assuming a 3D Gaussian distribution for the BOLD susceptibility changes

underlying the phase contrast. This assumption is arguably a good approximation for the sampling resolution of 3.75 x 3.75 x 4.5 mm^3 used in that study, but ignores the anatomical diversity of BOLD sources (e.g. large veins, parenchyma) and should be revised for higher spatial resolution. Furthermore, in a very recent study at 7 T, the observed phase and susceptibility changes in the cortex have been assigned to blood volume and oxygenation changes in pial and intracortical veins (Bianciardi et al., 2013).

The introduction of quantitative susceptibility mapping (QSM) (de Rochefort et al., 2008; Li and Leigh, 2004; Liu et al., 2009; Schweser et al., 2011; Shmueli et al., 2009; Wharton and Bowtell, 2010) has opened up new possibilities related to the use of phase images for fMRI studies. Quantitative susceptibility maps are calculated from phase data by deconvolution of field perturbations and hence, a voxel in the susceptibility map contains only the information about the respective voxel (i.e. without non-local effects). Provided that the phase effects from all susceptibility sources are detectable, susceptibility maps show the susceptibility changes that underlie magnitude signal changes in BOLD-based fMRI. Two recent reports (Bianciardi et al., 2013; Chen et al., 2013) propose the application of QSM for the quantification and better localization of functional BOLD contrast. Chen et al. (2013) proposed the use of susceptibility-based functional brain mapping by 3D-deconvolution of an MR-phase activation map, stating that the inversion of a phase t-score map is a reasonable solution for the purpose, as long as large phase angles can be ignored in the reconstruction. Such conditions are usually fulfilled for MRI acquisitions at short echo time, low field strength and low spatial resolution, and this approach has been applied to experimental data from a single subject to demonstrate the feasibility of the method. Bianciardi et al. (2013) generated QSM for each volume in the phase time-series of 2.5 mm isotropic fMRI data acquired at 7 T in order to compute activation related susceptibility change maps. They showed that functional, task related magnitude and phase changes can be detected with comparable sensitivity and that these changes have the same BOLD origins. The authors further demonstrated the feasibility of quantitative susceptibility mapping to estimate the functional change in blood fractional oxygen saturation in large veins (i.e. pial veins or sinuses) during task performance.

Here, we present a generalized approach for task-related BOLD susceptibility mapping, which we term functional quantitative susceptibility mapping (fQSM). We acquired high spatial resolution (1 mm isotropic) functional data at 7 T and combined these data across multiple orientations in order to provide a detailed comparison of the BOLD susceptibility contrast distribution with the magnitude BOLD contrast. We used different functional paradigms (motor, somatosensory and visual) in order to evaluate possible differences between BOLD responses in different brain areas. Several filter combinations for phase-specific artifact removal, QSM algorithms as well as alternative methods for the generation of statistical parametric maps were tested as integral parts of the multi-step fQSM pipeline. The final outputs of alternative fQSM pipelines were compared to results from standard magnitude based BOLD fMRI

analysis performed on the same complex datasets, relying on the expectation that a BOLD susceptibility shift generates an intensity change in the magnitude with opposite sign. Preliminary results of fQSM were presented at conferences and workshops (Balla et al., 2013a; Balla et al., 2013b; Balla et al., 2012).

2. Materials and methods

2.1 Subjects and experiments

Four experienced volunteers participated in this study, which was conducted with approval from the University of Nottingham Medical School Ethics Committee and all subjects gave their informed consent. All four subjects participated in a scan session in which multiple fMRI runs were carried out during a motor task. Each fMRI run was performed with the head rotated to a different angle relative to B_0 (MO datasets or multiple-orientation experiments). The mean rotation angles (± std) across subjects for each of the four rotations were: -8.9 ± 5.8° and 15.4 ± 6.8° achieved by nodding the head (single axis rotation around the right-left (RL) axis), and -14.4 ± 5.7° and 15.6 ± 3.0° relative to B_0, achieved by performing two-step rotations, first around the RL-axis and subsequently tilting the head sideways, corresponding to rotations around both the superior-inferior (SI) and anterior-posterior (AP) axes, respectively. Even though rotations around the SI axis (B_0-direction) do not have an influence on the image phase, rotation around the other two axes yield field distribution data whose inversion is less susceptible to noise propagation, provided the movement is restricted to small angles of revolution (Wharton et al., 2010). Three of these subjects also participated in an additional multi-task scan session during which three fMRI datasets were acquired using different brain activation paradigms (motor, somatosensory and visual) with the head held at the same orientation to the field (SO dataset or multi-task experiment).

2.2 Stimuli and paradigms

The motor task comprised a block paradigm of a visually-cued finger tapping task of the left hand for a period of 12 s, followed by a rest period of 18 s duration, repeated for ten cycles. In the multi-task scan session, block-paradigms using motor, visual and somatosensory stimulation were used. Visual stimuli were projected onto a screen positioned in front of the scanner and subjects viewed the screen through prism goggles and were instructed to focus on a centrally-located fixation cross. The paradigm consisted of presentation of 12 s of a flickering checkerboard ring stimulus extending from 2° to 2.75° (eccentricity) on a grey background alternating with 12 s of a full grey screen. This resulted in a 24 s cycle that was repeated 8 times. The somatosensory stimulus consisted of 60 Hz vibrotactile stimulation applied to all five fingertips of the left hand using five independently-controlled, MR-compatible piezoelectric devices (Dancer Design, UK). Each stimulator delivered a supra-threshold (~ 100 μm peak-to-peak amplitude) vibrotactile stimulus to ~1 mm^2 of the glabrous skin of each site. Analogous to the motor paradigm, blocks of 12 s of somatosensory stimulation alternated with blocks of 18 s of rest, for ten cycles. In total,

2 fMRI runs were carried out for the visual and motor paradigms, whilst 4 fMRI runs were performed for the somatosensory paradigm in order to compensate for the reduced fMRI signal modulation in response to sensory stimuli relative to visual or motor stimuli (Sanchez-Panchuelo et al., 2010).

2.3 Data acquisition

Experiments were performed on a 7 T scanner (Achieva, Philips, Best, Netherlands) using a volume birdcage RF resonator for transmission and a 32-channel coil-array for reception (Nova Medical, Wilmington, MA). Magnetic field inhomogeneity was minimized by using an image-based shimming approach (Poole and Bowtell, 2008). For the acquisition of functional time-series, high resolution (1 mm isotropic) multi-slice GE-EPI data were acquired with outer volume suppression in the phase-encoding direction (Feinberg et al., 1985; Pfeuffer et al., 2002a) and the following imaging parameters: TE/TR = 25/3000 ms, flip angle (α) = 85°, phase encoded (blipped) echo train length = 39, and parallel imaging (SENSE) acceleration factor = 2. The field-of-view (FOV) was 192 x 72 x 36 mm³ (AP-RL-HF / read-phase-slice) or 72 x 192 x 36 mm³ (AP-RL-HF / phase-read-slice) spanning the sensorimotor or visual cortex (Fig. 3a). In addition, a high resolution (0.7 mm isotropic) T_2*-weighted structural dataset covering the whole brain was recorded for each volunteer using a 3D-FLASH acquisition (TE/TR = 15/30 ms, α = 14°, blipped echo train length = 3, acceleration factor = 3) to serve as an anatomical references (Fig. 3a).

2.4 Data processing

A simplified depiction of the data processing pipeline is given in Fig. 1. This overview contains the most common processing steps at their most common positions in the pipeline, without the intention of suggesting the best recipe. Details of the pipeline components are provided below.

2.4.1 Preprocessing pipeline of the time-series

Magnitude and phase images of the fMRI datasets were reconstructed using the SENSE algorithm using the coil receive maps recorded in a separate reference scan. A brain mask was calculated by skull stripping the first volume of the magnitude datasets using the FSL Brain Extraction (BET) tool (Smith, 2002). This mask was applied to the phase images, which were then spatially unwrapped slice-by-slice using the PRELUDE option in FSL (Jenkinson, 2003) and temporally unwrapped voxel-wise using the unwrap function in Matlab. Motion correction matrices were calculated relative to the magnitude data of the first volume of the time-series using MCFLIRT (Jenkinson et al., 2002) with rigid-body transformations and normalized correlation as the cost function for minimization. Correction matrices were applied to the magnitude time-series using a final sinc-interpolation and separately to the unwrapped phase time-series using tri-linear interpolation for resampling. Different interpolation methods for magnitude and phase were used owing to the different characteristics of the phase and magnitude signal. The PSF of the magnitude signal can be mathematically described by a sinc function, and so will the

phase caused by externally imposed fields. However in practice, the phase values can vary between negative and positive values even within short distances. Therefore, in order to minimize the smoothing effect of the sinc function, we used tri-linear interpolation for the phase. This processing step was performed for each fMRI run separately. We investigated the use of four different, spatio-temporal filtering alternatives applied to the phase data. (i) The first involved temporal filtering of physiological noise effects using partial dynamic off-resonance correction in k-space (DORK) modified to include global bias removal (Hagberg et al., 2012; Pfeuffer et al., 2002b). Spatial filtering of low-frequency phase effects was achieved by using the sophisticated harmonic artifact reduction for phase data (SHARP) approach with a spherical deconvolution kernel of 2 voxels radius (2 mm) and a regularization parameter of 0.1 (Schweser et al., 2011). We will refer to this filter combination as DORK with SHARP. The three other alternative spatio-temporal filters were: (ii) complex regression of global phase changes in image space (NVR, (Hagberg et al., 2012)); (iii) 2D Gaussian homodyne high-pass filtering of the unwrapped phase with a filter width of 6 mm (homodyne, (Deistung et al., 2008; Haacke et al., 2004; Noll et al., 1991)) and (iv) removal of static phase components by complex division (Tomasi and Caparelli, 2007) in combination with 8th order 2D polynomial high-pass filtering of the resulting relative phase images (RELPOLY, (Bianciardi et al., 2011)). The time-series from the multiple fMRI runs were co-registered using the FLIRT tool (Jenkinson et al., 2002) by aligning the motion correction reference volumes (i.e. the first dynamic of the modulus data time-series) using 12-parameter affine transformations and by employing normalized correlation as the cost function for the minimization process. The reference dataset was the first volume acquired in the experiment (i.e. for MO datasets the first volume along the first orientation). For both magnitude and phase data tri-linear interpolation was applied for resampling. In rare cases (n = 4), where this alignment failed, modification of parameter limits, alternative cost functions (absolute Pearson correlation or mutual information) or brain masks that avoided frontal regions of the brain were used.

2.4.2 Processing of QSM time-series

The preprocessed phase images (in units of radian) were transformed into field maps (in ppm) by dividing by the factor $\gamma B_0 TE \cdot 10^{-6}$ prior to QSM computation. For the QSM algorithm, knowledge of the exact orientation of each dataset relative to B_0 is required. This information was obtained from the normalized 3 x 3 rotation matrix $R = R_{seq}$ and $R = R_{reg}^{-1} \times R_{seq}$ for SO and MO datasets, respectively. R_{seq} is a rigid-body rotation matrix derived from the slice angulation parameters in the Philips PAR-file and R_{reg} is the upper left of the affine FLIRT co-registration matrix between the different orientations of the MO dataset. The reconstruction of QSM series for MO datasets was performed using the regularized COSMOS algorithm (Liu et al., 2009; Wharton and Bowtell, 2010), whilst for SO datasets a regularized iterative algorithm using edge information derived from the modulus data (RSO, (de Rochefort et al., 2010; Wharton and Bowtell, 2010)) and the threshold-based k-space division approach (TKD, (Shmueli et al.,

2009; Wharton et al., 2010)) were used. QSM time-series were demeaned, concatenated to include scans acquired with the same functional paradigm and high-pass filtered in the temporal domain with a FWHM of 1.5 times the block repetition period of the stimulation paradigm. Demeaning avoided susceptibility jumps due to concatenation of the time-series of consecutive fMRI scans. A constant value of 100 ppm was also added as a general offset, as this was necessary to include negative susceptibility values in the analysis (since the FEAT tool (Woolrich et al., 2001), developed for magnitude data, masks any negative voxels prior to fitting of the general linear model (GLM)).

2.4.3 Processing of activation maps

Statistical parametric maps (SPM) were calculated for susceptibility, phase and modulus fMRI time-series data using FEAT. The GLM used the functional paradigm convolved with a double-gamma hemodynamic response function (HRF). The GLM also included the derivative of the first component in order to take account of small differences in the timing of the haemodynamic response. Resulting t-score maps were used for analysis (e.g. common voxel diagrams, see below). Although all analyses were performed on maps in their processed form in the EPI-space, the filtered parameter estimate maps were overlaid on the anatomical reference datasets for illustrative purposes.

2.4.4 Common voxel masks and diagrams

In order to present and compare the magnitude BOLD fMRI and fQSM results, the latter being produced for a range of pipelines for comparison, we computed common voxel masks and diagrams. For a given significance threshold, a common voxel mask was formed by identifying voxels that showed significant activation in two SPMs. Common voxel diagrams are boxplots where individual groups contain the common voxel ratios (i.e. number of common voxel / number of significant voxels) across the subjects at a given significance threshold (e.g. t-score).

2.4.5 Processing of anatomical reference QSMs

In order to produce anatomical reference QSMs, whole-head FLASH phase data were first spatially unwrapped using a fast 3D algorithm (Abdul-Rahman et al., 2007) and then high-pass filtered, using two different methods: (i) SHARP using a kernel radius of 6 voxels (6 mm) and a regularization threshold parameter of 0.2 (Schweser et al., 2011); (ii) the combined application of a 2nd order, 3D polynomial high-pass filter and an iterative dipole deconvolution algorithm, based on L_2-norm minimization (de Rochefort et al., 2010; Wharton and Bowtell, 2010). The use of SHARP with a large kernel radius yielded excellent filter performance at the cost of no filtering on the external part of the brain over a region whose extent was approximately equal to the kernel size. The dipole deconvolution filter performed well in external regions, but was less efficient than SHARP in the lower mid-brain regions due to the effect of B_1^+ inhomogeneities (Schweser et al., 2011). Hence, filtered phase data results using SHARP and the dipole deconvolution filter were combined to produce full coverage of the brain by replacing voxel values set to

zero by SHARP with values generated by the dipole deconvolution. This combined dataset was used as input to the QSM calculation, which was based on the same regularized approach that was used for the functional SO fMRI datasets (de Rochefort et al., 2010; Wharton and Bowtell, 2010).

3. Results

3.1 The BOLD contrast in phase time-series

Figure 2 presents parameter estimates (paradigm-related contrast change) of the GLM-fit of the phase time-series to the functional paradigm, in the case where no complex temporal and spatial filtering nor QSM calculation were applied in the phase processing pipeline (Fig. 1). The coronal and sagittal slices in Fig. 2a and 2b illustrate an artifact caused by the 7 T magnet's cryogenic-pumps, which is a sinusoidal wave with a 2 Hz frequency, travelling in and out of the image in the head-foot direction. The frequency was derived from the temporal separation of global image phase minima, which is the time needed for the acquisition of 6 slices, corresponding to 0.5 seconds (indicated in Fig.2b). This travelling wave pattern, exemplified in Figs. 2a and 2b, was observed in all phase time-series acquired with sequential 2D slice sampling. However, the artifact is negligible for the modulus time-series of the same complex dataset. This demonstrates that the spatial and temporal MR phase contrast is more sensitive to external large-length-scale field perturbations than the modulus contrast, and suggests that phase time-series and their derivatives (e.g. frequency-map or QSM series) need special filtering for an efficient exploration of BOLD contrast. This kind of artefact is not unique to 7 T systems and has been observed in phase images acquired at 3 T (Hagberg et al., 2008). We expect the travelling wave artifact to appear in data acquired using similar high-field-magnets with cold-heads, but the detailed appearance of the artefact will depend on several experimental factors (e.g. shielding of the magnet, arrangement of gradient and shim coils, slice sampling order etc.). Figures 2c-f show the functional BOLD contrast in a transverse plane of four datasets acquired at different orientations (Subject 1, MO datasets). The maps in Figs. 2d-f are eroded on the edges, since they were calculated for phase time-series with partial head coverage, which were spatially registered to the dataset acquired with the head in the first orientation. Figure S1 (Supplementary Material) presents the $\Delta\phi_B$ activation maps of the same dataset calculated using spatio-temporal filtering with DORK and SHARP, significance masking at t = 2.3 and spatial projection onto the anatomical reference. The static non-local effects due to varying magnetic susceptibilities make it difficult to interpret the results from functional phase or frequency mapping and fQSM can help in the interpretation of these maps.

3.2 BOLD contrast characteristics in fQSM compared to magnitude BOLD fMRI

Figures 3b and 3c show representative phase maps ($\Delta\phi$) and QSM ($\Delta\chi$), reconstructed from a single complex zoomed EPI dataset in a functional time-series covering the visual (Fig. 3b) and somatosensory /

motor (Fig. 3c) regions. Statistical parameters were estimated from the series of such maps. The fQSM and fMRI t-score maps were arbitrarily thresholded at $t = 2.3$ and the results binarized in order to generate masks of "significant" voxels for each. Significant parameter estimate maps ($\Delta I_B /\bar{I}$ and $\Delta\chi_B$) overlaid onto magnitude images are presented in Fig. 3d. Those voxels which were significant in both fQSM (or phase fMRI) and magnitude fMRI maps were then used to build a second "common" voxel mask. After significant or common voxel masking, projections of parameter estimates for BOLD susceptibility and magnitude changes were overlaid onto the anatomical reference QSMs for display. Further thresholding was done directly on the masked and projected parameter estimate maps (see scale bars in Figs. 4 - 6). Figure 4 shows the reference $\Delta\chi$ maps, with common voxel masked $\Delta\chi_B^{com}$ and significant voxel masked $\Delta I_B /\bar{I}$ overlays for a representative transverse slice for each subject produced using the DORK with SHARP filter combination in the processing pipeline for MO datasets. By showing these common and significant voxel masked overlays, the intention was to illustrate, besides quantitative activation related BOLD contrast, also the sensitivity of fQSM relative to magnitude BOLD fMRI at a commonly used significance threshold level ($t = 2.3$). The dominant BOLD contrast foci both in $\Delta I_B /\bar{I}$ and $\Delta\chi_B^{com}$ maps are located in the banks of the central sulci (paramagnetic areas in the reference QSMs) likely resulting from susceptibility changes in pial veins. The highest and relatively sharp diamagnetic $\Delta\chi_B^{com}$ peaks are co-localized with the positive $\Delta I_B /\bar{I}$ peaks. $\Delta\chi_B^{com}$ changes in cortical voxels neighboring the CSF are diamagnetic, whereas voxels in deeper cortical layers usually show a paramagnetic susceptibility shift in Fig. 4.

Figure 5a-c presents results for a selected transverse slice from a SO dataset involving visual stimulation for Subject 1. Example results of experiments using the somatosensory paradigm are also presented for selected transverse (Fig. 5d-e) and sagittal slices (Fig. 5f-g). Lower thresholds for masked and projected parameter estimates (0.01 ppb for fQSM and 0.1% for fMRI) were used in the somatosensory data due to the weaker contrast produced by this functional paradigm. Figures 5d and 5f demonstrate that even at these lower contrast levels, fQSM has enough sensitivity to detect activation in the parenchyma, and the quality of $\Delta\chi_B^{com}$ maps is comparable to the quality of $\Delta I_B /\bar{I}$ maps (Fig. 5e and 5g). Figure 6 presents the maps in selected slices of the visual and somatosensory cortex where the modulus BOLD contrast was dominantly negative (Fig. 6b shows the corresponding $\Delta\phi_B^{com}$ map for the visual paradigm). On inspection, the phase fMRI map has comparable quality to the fQSM, though the local values differ in most activated voxels. Between the fQSM and magnitude fMRI maps the expected relationship (magnitude BOLD contrast due to susceptibility changes of opposite sign) is easily observed, but the distribution of common voxel values in phase fMRI maps is difficult to interpret by comparison to the other two types of BOLD maps. Figure S2 presents the comparison of SO fQSM results for the three different functional paradigms applied at a significance threshold $t = 2.3$. Although the differences in the

common voxel ratios (Fig. S2a) are clearly observable, we show below that they depend on the significance threshold and therefore, these diagrams do not allow general conclusions to be drawn.

Figure 7 plots $\Delta\chi_B^{com}$ values as a function of $\Delta I_B^{com}/\overline{I^{com}}$ for each voxel in the common mask in order to allow visualization of the distribution of susceptibility and modulus changes and the voxel-wise covariance of the two parameters. An unexpectedly large amount of voxels were found in quadrants I and III, where the observed modulus BOLD contrast and susceptibility change have the same direction. In the case of the motor-task, the voxels in quadrant I can be assigned to the paramagnetic $\Delta\chi_B^{com}$ regions observed in the parenchyma in Fig. 4. This finding was reproduced with the same functional paradigm in the independent SO experiments (Fig. 7b). The relative proportion of such voxels in the data from the visual and somatosensory paradigms was less (Figs. 7c and 7d). Figure S3 shows the histograms of the individual $\Delta I_B/\overline{I}$ and $\Delta\chi_B^{com}$ maps. The coefficients of correlation between the positive $\Delta I_B^{com}/\overline{I^{com}}$ and diamagnetic $\Delta\chi_B^{com}$ values of common voxels together with the length of the time-series in time-points are summarized in Table 1. We observe that higher number of time-points increases the related correlation coefficients.

3.3 Effects of the significance threshold and spatio-temporal filtering in fQSM

Four spatio-temporal fQSM pipeline filters were compared based on the ratio of the number of common voxels to the total number of significant magnitude (fMRI) and susceptibility (fQSM) voxels identified using significance thresholds of t = 2.3 and t = 4 (Fig. 8). The bar-plots show the mean percentage values over the four subjects with the error bars indicating standard deviations. In Fig. 8a and 8b the norms were the numbers of all fMRI voxels (stacked bar plot), whereas in Fig. 8c and 8d the number of common voxels were normalized by using the number of fQSM voxels with similar sign (grouped bar plots). Stimulation-related susceptibility changes are detected in ~40 - 50% of ΔI_B voxels in data that were not subjected to filtering, and this ratio is even smaller for filtered data (Fig. 8a-b), indicating a reduction of the fQSM detection limit relative to fMRI magnitude sensitivity when spatio-temporal filtering is applied. Comparing the bar plots at different significance thresholds, we find that at the higher threshold level the ratio of the number of significant fQSM to fMRI voxels decreases, meaning that the t-scores of fMRI SPMs are generally higher than the t-scores of fQSMs. Figure 8c and 8d shows the common voxels normalized to the total number of positive or negative fQSM voxels, and in contrast to Fig. 8a and 8b indicates how spatially reliable (rather than how sensitive) the SPMs found with fQSM are. The bar plot for t > 2.3 (Fig. 8c) indicates that spatio-temporal filtering improves the spatial reliability of fQSM, at least for voxels with negative BOLD susceptibility contrast ($\Delta\chi_B$).

Figure 9 presents the common voxel diagrams for different QSM calculation approaches (no QSM – phase fMRI, SO TKD and RSO, MO COSMOS) and for DORK with SHARP spatio-temporal filtering relative to no spatio-temporal filtering. A common feature in all diagrams is the rapid decrease of the

11

common voxel ratio between t = 0 and 2. Generally, with t > 2 the negative (diamagnetic) common voxel ratio starts to recover, until the positive voxel ratio mostly stagnates or even further decreases. Without the application of a phase filter (Fig. 9, MC label), the recovery of the negative ratio is reduced and the positive ratio shows a slight upwards trend. For SO phase activation maps (Fig. 9, "ph" label meaning no QSM), the upwards trend is even more pronounced, whether or not phase filtering was applied, leading to a reduced divergence between the negative and positive curves. Both single orientation QSM algorithms (TKD and RSO) produce very similar diagrams (see Fig. 3 and S4 for a direct comparison using masking with t > 2.3). The interested reader can find the brief summary of a comparison of 30 alternative fQSM pipelines based on common voxel diagrams in the Supplementary Material (Fig. S5). This comparison additionally treated pipeline concepts deviating from those presented in Fig. 1, involving superfast dipole inversion (SDI,(Schweser et al., 2012a)) instead of spatio-temporal filtering and QSM calculation, and independent component analysis (ICA,(Beckmann and Smith, 2004)) instead of spatio-temporal filtering and GLM-fitting.

4. Discussion

In this study we investigated the local source of the complex functional BOLD contrast using several reconstruction pipelines and functional paradigms. The goal was to analyze the potential and establish fQSM as a partner for magnitude BOLD fMRI, providing complementary information on BOLD susceptibility changes derived directly from the same complex dataset.

4.1 Multiple orientation fQSM: validation of SO fQSM

In anatomical QSM, multiple-orientation experiments reconstructed with the COSMOS algorithm (Liu et al., 2009) are considered to be the gold standard and such experiments are often used as reference for the validation of SO results. This is due to the unique solution of the inverse relationship between susceptibility and phase offered by the combination of at least 3 complex datasets of the same object oriented at different angles to the main magnetic field. In this study we used 4 orientations employing rotations along two different axes because of the benefits this offers in the inversion accuracy (Wharton and Bowtell, 2010). Hence, we consider the MO results presented here as the best case scenario for fQSM at 7 T and use them for validation of the SO fQSM results. The comparisons presented in Figs. 7 and 9 demonstrate that MO fQSM outperforms SO fQSM in accuracy, presumably due to the better contrast to noise in the case of MO data. However, the noise enhancement for SO techniques is well-known for anatomical QSM as a feature of the ill-posed inversion problem and, as such, cannot be totally avoided with state-of-the-art algorithms. Nevertheless, SO susceptibility SPMs are very similar to MO SPMs for the motor paradigm, even if the SO dataset was obtained on a different day to the MO dataset (Fig. 7). This suggests that conclusions drawn from MO fQSM results are valid for SO fQSM. Differences

between SO and MO fQSMs due to static orientation effects in SO QSM (Fan et al., 2013) were not considered here. Such orientation effects are difficult to distinguish from physiological variability across repeats and registration artifacts (Fig. S6). Generally, BOLD activation consists of a large contiguous brain area that undergoes susceptibility changes owing to an increase in the local blood oxygenation fraction. Both the capillaries at the level of the cortical layers and the pial veins undergo such changes. The concerted action of these structures driving the BOLD effect, leads to an over-all non-cylindrical shape of the activated area. Our results indicate that the SO fQSM of such areas is less prone to orientation dependent effects, than in voxels assigned to vascular structures (Figs. S6 and 3 - 6).

4.2 Alternative fQSM pipelines

The choice of spatio-temporal phase filtering modalities and the parameter settings used for application in fQSM in this study were selected based on previous publications and several preliminary trials. Essential arguments for the selection were: DORK and NVR are dynamic and spatially *global* phase corrections, RELPOLY removes the static contrast, homodyne filtering introduces a *uniform* spatial weighting of the phase time-series and SHARP modifies only phase components with external origins and leaves the local intrinsic phase untouched. Potentially useful spatial filtering methods omitted in the comparison presented both in the manuscript and the supplementary material were the static background phase removal based upon an iterative dipole deconvolution filter (de Rochefort et al., 2010; Wharton and Bowtell, 2010), RESHARP (Sun and Wilman, 2013), V-SHARP (Wu et al., 2012) and HARPERELLA (Li et al., 2014). The iterative dipole deconvolution method and RESHARP provided filtered phase images of comparable quality to SHARP, with corrected phase values also in voxels cropped by SHARP, but they were significantly less time efficient. V-SHARP also yielded phase maps of comparable quality to SHARP without substantial speed penalty. Yet generally, we found SHARP with a kernel size of 2 voxels fast and robust for the application on our spatially zoomed time-series, cropping only a minimal number of voxels close to the brain edge, which at the resolution of 1 mm³ was not critical. Perhaps the most widely used temporal filtering technique used for physiological noise removal is RETROICOR (Glover et al., 2000). The reason for not including RETROICOR in our comparison was the lack of physiological recordings (real time breathing and heartbeat curves) during the experiments. Furthermore, in a previous study Bianciardi et al. (2013) compared RETROICOR to a novel filter combination broadly matching one composed of NVR and RELPOLY, and found that their filter combination was more efficient in removing physiological noise. Hagberg et al. (2012) comprehensively analyzed and compared several physiological noise filters for complex time-series and also found that homodyne filtering, NVR and a modified version of DORK outperformed RETROICOR. We implemented NVR and the modified DORK as proposed in that paper, combining the latter with the spatial SHARP filter. The comparison of alternative pipelines with different spatio-temporal filters presented here was based on consideration of the number of common voxels in the final activation maps. Results suggest that spatio-temporal filtering of the phase is pivotal

for fQSM, otherwise a large proportion of the significant fQSM voxels are not common (i.e. do not show significant activation in the magnitude-based SPMs, see Fig. 8c-d). Activation maps calculated using fQSM pipelines with 2D Gaussian high-pass filtering, RELPOLY and DORK with SHARP resulted in comparable common voxel ratios. Hence, it may be hypothesized that each of these filters efficiently removed the spatially varying component of the phase from sources outside the brain and reduced the temporal phase fluctuations to levels where activation-related BOLD changes could be detected. Identification of the optimal approach from these three spatio-temporal filtering alternatives is difficult without knowledge of the true susceptibility changes during activation, and it is not in the scope of this study to propose a pipeline with fixed steps. However, we believe that the removal of background fields due to external phase contrast sources and the correction for dynamic changes in the global phase contrast (e.g. the travelling wave artefact induced by the cryogenic-pumps, see Fig. 2) using DORK with SHARP is a superior alternative to high-pass filtering that removes more phase contrast from local (brain tissue) sources. A comparison made at the significance threshold of t = 2.3 showed that although homodyne (Gaussian high-pass) filtering was very efficient in noise reduction, it decreased $|\Delta\chi_B^{com}|$ values by 27 $\pm$ 12 % relative to the DORK with SHARP combination. Similarly, we compared different single orientation QSM algorithms as integral parts on the fQSM pipeline and found minimal advantages for the edge-regularized inversion method (RSO) relative to the thresholded k-space division method (TKD), based on the inspection of the common voxel diagrams (Fig. 9). The origin of differences can be tentatively attributed to the well-known noise enhancement in TKD generated QSMs (Wharton and Bowtell, 2010). It has to be noted though that the only parameter compared was the number of common voxels, which indicates differences and similarities in sensitivity and spatial reliability, but provides no information on the accuracy of quantification. BOLD quantification using RSO-type algorithms can be biased by the a priori information used for regularization of the inversion process (Wharton and Bowtell, 2010), though we believe that RSO is favorable for the application on SO time-series to TKD. The development of novel RSO-type algorithms optimized for more accurate and faster processing of QSMs is an active field of research and fQSM benefits directly from every improvement on this field, e.g. (Bilgic et al., 2013; Schweser et al., 2012a; Schweser et al., 2012b; Wu et al., 2012). Thus, we suggest the implementation of the fQSM pipeline for SO datasets using DORK with SHARP spatio-temporal phase filtering and regularized QSM calculation algorithms using a priori information about edges in the object derived from the magnitude image.

4.3 Noise, sensitivity and spatial reliability of fQSM

Noise in functional susceptibility change maps propagates from the phase time-series and, therefore, fQSM data are more likely to be affected by stimulus-independent dynamic physiological changes than modulus activation maps (Hagberg et al., 2008; Petridou et al., 2009). This effect, which arises in part from the different contrast caused by the same susceptibility distribution in phase and magnitude images,

can be reduced by increasing the spatial resolution, if the signal to thermal noise ratio is sufficient (Petridou et al., 2009). In line with this, an essential aspect of the present study relative to previous studies on activation-related BOLD phase (Arja et al., 2010; Bianciardi et al., 2011; Feng et al., 2009; Hagberg et al., 2008; Hagberg et al., 2012; Menon, 2002; Petridou et al., 2009; Rowe et al., 2007; Tomasi and Caparelli, 2007) and BOLD susceptibility changes in humans (Bianciardi et al., 2012; Bianciardi et al., 2013; Bilgic et al., 2013; Chen et al., 2013), is the increased spatial resolution (1 mm isotropic) and the deliberate avoidance of spatial smoothing. Both the number of activated voxels and the number of common voxels increased significantly when the fMRI data were spatially smoothed before the GLM fit (Balla et al., 2012). However, smoothing has a dramatic effect on the parameter estimates: Gaussian smoothing with a filter width of 2 times the voxel size changes ΔI_B, $\Delta\phi_B$ and $\Delta\chi_B$ in some regions by more than 300%. Thus, smoothing was excluded from the fQSM processing pipeline to improve quantification and to retain the effective spatial resolution. Nevertheless, if quantification and high spatial sampling resolution are not important, smoothing can be used to trade spatial resolution for signal to non-physiological (i.e. thermal) noise, thereby improving the statistical analysis.

We can determine the sensitivity of fQSM relative to fMRI using the common voxel ratios normalized to the total number of fMRI voxels. Based on our results, this relative sensitivity decreases with increasing significance thresholds (Fig. 8a-b and 9) and also decreases after efficient spatio-temporal filtering (i.e. when phase "noise" is reduced). The value for fQSM with phase filtering was $35 - 40$ % using $t > 2.3$ and $25 - 30$ % using $t > 4$. A source of sensitivity loss in fQSM and phase fMRI compared to magnitude fMRI is that no T_2-contrast is expected either at single time-points or in the time-series. T_2 relaxation is driven by molecular motion on the microscopic level and is manifested as a decay of the average magnitude signal without an average phase effect. Susceptibility sources under the detection limit of fQSM (e.g. in parenchyma) can still produce a significant BOLD T_2-contrast in fMRI. However, the results of this study suggest that this detection limit can be pushed sufficiently low to detect even weak activations (<0.1 ppb) in the parenchyma by acquiring longer time-series for the GLM fit. The minimum detectable susceptibility changes in this study at a significance threshold of $t = 2.3$ were 0.021 ppb for motor, 0.026 ppb for visual and 0.016 ppb for somatosensory stimulation protocols, depending partly on the number of images in the time-series and partly on the activation paradigm and region (see Fig. S2). A further source of sensitivity loss in fQSM and phase fMRI is the higher physiological noise contribution in phase images. This was minimized in the present study by the relatively high spatial resolution (Petridou et al., 2009) and the optimized preprocessing pipeline. Finally, a source of sensitivity loss specific for fQSM, which is not present in phase fMRI, is the absence of non-local contrast contributions due to projected fields. This sensitivity loss is analogous to that expected in spin echo fMRI relative to gradient echo fMRI and is a direct trade-off for better contrast specificity.

Spatial reliability of functional susceptibility maps was defined here by the ratio of the number of common voxels and the number of significant fQSM voxels bearing a susceptibility shift value with the same sign (Fig. 8c-d). A substantial enhancement of spatial reliability was observed for the voxels with diamagnetic shifts when using efficient spatio-temporal filters and the trend increased as the significance threshold was increased. Interestingly, no such effects were observed for voxels with paramagnetic shifts. In Fig. 9 and Fig. S5 it becomes clear that this kind of divergence between the diamagnetic and paramagnetic voxels appears only in fQSM, not in phase fMRI. Supposed paramagnetic susceptibility shifts generate a negative magnitude BOLD contrast, negative $\Delta I_B^{com}/\overline{I^{com}}$ are expected to appear as often as paramagnetic $\Delta\chi_B$ values, which is not the case according to our results (Figs. 4-7). Instead, paramagnetic $\Delta\chi_B$ values were detected in the deep layers of the motor cortex in all subjects (Fig. 4) and in other regions (Fig. 5-6). A particular feature of voxels with paramagnetic $\Delta\chi_B^{com}$ and positive $\Delta I_B^{com}/\overline{I^{com}}$ (see Fig. 7) is that $\Delta I_B^{com}/\overline{I^{com}}$ is on average lower than in voxels with diamagnetic $\Delta\chi_B^{com}$ (e.g. in cortical layers close to white matter or in tissue adjacent to draining veins – see Fig. 4-7). Hence, we interpret this observation as a sign inversion of fQSM values (Figs. 4 and 7) in voxels where the local static and dynamic phase contrast is close to the noise level (e.g. in the parenchyma) and close to strong dynamic field perturbation sources (e.g. veins draining from active tissue). The divergence between diamagnetic and paramagnetic common voxel ratios in fQSM, which is not present for phase fMRI (Figs. 9 and S5), indicates that: (i) non-local phase contrast components before QSM processing were dominant in voxels in quadrants I and III (Fig. 7); (ii) after the deconvolution of non-local static phase components (i.e. the QSM processing step in the fQSM pipeline) the activation-related contrast in such voxels has the opposite sign than expected. The unexpected sign change appeared for all QSM algorithms used in the fQSM pipeline (i.e. COSMOS, RSO, TKD and SDI) and therefore, it is an intriguing issue that motivates further investigations.

4.4 Potentials and pitfalls

The main motivation for developing fQSM is that significant parameter estimate maps have a more direct quantitative and spatial relation to the physiological BOLD effect than magnitude BOLD fMRI SPMs. Where the oxygen surplus provided by increased cerebral blood flow (CBF) dominates the increase in the tissue's oxygen extraction fraction (1-Y) and the regionally increased venous blood volume (CBV), diamagnetic $\Delta\chi_B$ and positive $\Delta \mathbf{I_B}/\overline{\mathbf{I}}$ contrast is expected. It is also expected that in some regions this balance is shifted and paramagnetic $\Delta\chi_B$ with negative $\Delta \mathbf{I_B}/\overline{\mathbf{I}}$ appear. Our results showed that for different subjects and methods, in most of the significant voxels these expectations are met (Fig. 7). The voxels where expectations were met could be tentatively assigned to pial and intracortical veins as well as cortical layers close to the pial surface by inspection of the anatomical references (Fig. 4-6). However, in a substantially high number of voxels the above mentioned expectation were not met (Fig. 7), due to a sign change of the contrast and those voxels were assigned mainly to brain tissue distant from the pial

surface. .Another issue with fQSM in brain tissue is that it may be difficult to separate the contribution of fractional oxygen saturation changes from that of CBV changes to the measured $\Delta\chi_B$ (Bianciardi et al., 2013). Yet, in voxels embedded in vascular compartments, $\mathbf{CBV_{act}^{vox} = CBV_{rest}^{vox}}$ and $\Delta\chi_B^{vox} = \Delta\chi_B^{max} \cdot \mathbf{Hct} \cdot (\mathbf{Y_{rest}^{vox} - Y_{act}^{vox}})$, where act indicates "on activation", rest indicates "on rest", $\Delta\chi_B^{max}$ is the susceptibility difference between fully oxygenated and deoxygenated blood and *Hct* is the fractional hematocrit in the vein. The latter relation was used for the estimation of functional oxygenation changes in large veins of the visual cortex (Bianciardi et al., 2013) and in pial veins of the motor cortex in humans (Haacke et al., 1997; Haacke et al., 1995; Hoogenraad et al., 1998). The 2013 study was performed at 2.5 mm isotropic resolution, and involved removal of non-local phase effects. It reported an activation-induced susceptibility change of -3.5 ± 0.6 ppb corresponding to a blood oxygenation change of 0.048 ± 0.009 in the sagittal sinus, calculated with $\Delta\chi_B^{max} = 4\pi \cdot 0.18$ ppm (Weisskoff and Kiihne, 1992) and *Hct* = 0.4. In early studies in motor cortex, performed at high spatial resolution (0.5 x 0.5 x 1 mm³), susceptibility was determined without deconvolution of non-local phase effects, but the calculation was restricted to voxels where phase changes due to activation of external origin could be ignored relative to local effects yielding a susceptibility change of -10 ppb (corresponding to an oxygenation change of 0.14) in pial veins. In the present study, a search for voxels apparently embedded in pial and intracortical veins was performed using the MO motor dataset of Subject 1 and resulted in susceptibility changes ranging from -14 to -30 ppb, which corresponds to an oxygenation change of 0.16 to 0.33. Differences with the previous studies can arise from the downstream dilution of activation related oxygenation changes in the investigated veins (Turner, 2002), volume averaging effects due to the diverse sampling resolutions applied or in selection criteria used for identifying veins.

5. Conclusion

Blood susceptibility changes due to neural activation were mapped with fQSM and were compared to magnitude and phase BOLD fMRI results from the same complex time-series. The high spatial resolution of the data allowed for the detection of phase contrast that would otherwise be cancelled by spatial averaging at coarser resolution. Detection of such subtle phase changes was important, since susceptibilities can only be mapped if their non-local phase effects are observed. The comparison of several fQSM pipelines indicated that spatio-temporal filtering of the phase data is essential for generating good quality fQSM, but the number of coincidentally significant voxels in fQSM and fMRI did not vary considerably for most of the tested filters. Multiple orientation datasets produced the best fQSMs, which were used to validate single orientation fQSM results. The sensitivity of fQSM was calculated to be ~25 – 40 % relative to magnitude BOLD fMRI and found to depend strongly on the significance thresholds used in forming the SPMs. The spatial reliability of fQSM voxels also depends on the significance threshold, however, until the relative sensitivity of fQSM to fMRI decreases with the

threshold, the relative spatial accuracy increases with it. The reliability of fQSM in quantifying susceptibility changes was not analyzed here, as this would have required knowledge of the magnitude and sign of those changes. Therefore, future studies will address the accuracy of quantification with fQSM, with the aim to understand the observed sign inconsistency in cortical layers close to the white matter. Given the fundamental differences between magnitude and susceptibility BOLD (fMRI and fQSM) contrast, the information in fQSM can be considered as complementary to that in fMRI. Our results suggest that fQSM yields quantitative intra-vascular BOLD contrast and, hence, increasing the spatial resolution is expected to increase the specificity of fQSM towards smaller vessels and make quantitative BOLD with even higher neural activation specificity possible.

6. Table legends

Table 1

Correlation coefficients between the positive $\Delta I_B^{com}/\overline{I^{com}}$ and diamagnetic $\Delta \chi_B^{com}$ values of common voxels. The effective numbers of time-points in the evaluated fMRI and fQSM time-series are indicated. For MO time-series the components acquired in different orientations were concatenated for fMRI or combined with COSMOS for fQSM.

7. Figure legends

Figure 1

Illustrative scheme of the fMRI and fQSM pipelines with the processing steps at their most usual locations.

Figure 2

BOLD phase change maps in radians from the MO dataset of Subject 1 demonstrating phase-specific artifacts. (a) coronal, (b) sagittal and (c) transverse sections with the head rotated along the first angle. (d), (e) and (f) transverse sections from the three other SPMs calculated from time-series with the head rotated in different orientations. The time-series were projected into the space of the dataset along the first angle before the GLM-fit. Due to the partial head coverage of the zoomed-EPI acquisition, image regions in the reference space which were not sampled with the head rotated in different orientations are not visible (d-f). Particular image regions where the processing artifacts can be followed are indicated by arrows in (c)-(f).

Figure 3

Representative parameter maps calculated from the complex time-series acquired from Subject 1. (a) Sagittal (left) and coronal (right) projection of the zoomed slice packages covering the main visual and

motor / somatosensory neural centers in the brain (colored) overlaid onto the reference 3D scan. (b) Brain tissue induced phase contrast in the visual cortex spatially filtered using SHARP (left, 3rd repetition in time-series, slice containing parts of V1) and corresponding QSM, calculated using the RSO algorithm (right). (c) Intrinsic phase contrast in the motor cortex using SHARP filtering (left, 3rd repetition in time-series acquired along the first orientation of the MO experiment, slice containing parts of M1) and QSMs calculated using the indicated methods (right). (d) Modulus (left) and susceptibility (right) BOLD contrast (fQSM pipeline using DORK with SHARP phase filtering) masked using the significance threshold of t = 2.3, but not the "common voxel" constraint, and overlaid onto the modulus image of the slice shown in (c).

Figure 4

Common MO susceptibility ($\Delta\chi_B^{com}$) and relative magnitude ($\Delta I_B /\bar{I}$) parameter change maps for the motor paradigm co-registered with, and overlaid on, high-resolution anatomical reference QSMs ($\Delta\chi$). Magnitude maps were generated by combining datasets across the MO datasets. Selected transverse slices for MO motor datasets from (a) Subject 1, (b) Subject 2, (c) Subject 3, (d) Subject 4. A – anterior, P – posterior, R – right, L – left.

Figure 5

Parameter maps for the SO visual and somatosensory experiments on subject 1. Visual paradigm results: (a) selected transverse slice from the QSM reference; (b) common susceptibility change map ($\Delta\chi_B^{com}$) and (c) relative modulus intensity change map ($\Delta I_B /\bar{I}$). Color bars for subplots (a-c) are specific for the parameter maps they are flanking. Somatosensory paradigm results: (d) transversal $\Delta\chi_B^{com}$ map; (e) transversal $\Delta I_B /\bar{I}$ map; (f) sagittal $\Delta\chi_B^{com}$ map; (g) sagittal $\Delta I_B /\bar{I}$ map. A – anterior, P – posterior, R – right, L – left, S – superior, I – inferior.

Figure 6

Parameter maps for the SO visual and somatosensory experiments on subject 1 for slices where negative magnitude BOLD dominated. Visual paradigm results: (a) selected transverse slice from the QSM reference; (b) common phase change maps ($\Delta\phi_B^{com}$); (c) common susceptibility change map ($\Delta\chi_B^{com}$) and (d) relative modulus intensity change map ($\Delta I_B /\bar{I}$). Color bars for subplots (a-c) are specific for the parameter maps which they flank. Somatosensory paradigm results: (d) axial $\Delta\chi_B^{com}$ map; (e) axial $\Delta I_B /\bar{I}$ map; (f) sagittal $\Delta\chi_B^{com}$ map; (g) sagittal $\Delta I_B /\bar{I}$ map. Color bars flanking subplots (d) and (e) show the scaling for somatosensory $\Delta\chi_B^{com}$ maps, whereas those flanking subplots (f) and (g) are related to the somatosensory $\Delta I_B /\bar{I}$ maps. A – anterior, P – posterior, R – right, L – left, S – superior, I – inferior.

Figure 7

Scatter plots of all relative magnitude ($\Delta I_B^{com}/\overline{I^{com}}$) and susceptibility changes ($\Delta\chi_B^{com}$) at common voxels positions. (a) MO datasets; (b) SO motor datasets; (c) SO visual datasets; (d) SO somatosensory datasets.

Figure 8

Common voxels stacked bar plots for different filters and for (a) t > 2.3 and (b) t > 4.0, normed with the total number of fMRI voxels. Grouped bar plots for (c) t > 2.3 and (d) t > 4.0, normed with the number of + or – fQSM voxels.

Figure 9

Common voxel diagrams for fQSM pipelines with different QSM calculation methods (no QSM, TKD, RSO and COSMOS) and different spatio-temporal phase filters (DORK with SHARP vs. no filtering). The SO vs. MO comparison is facilitated by showing the diagrams for one out of four SO component in a MO dataset (4th orientation) and the diagrams for the combined MO datasets (COSMOS). Blue – voxels with negative contrast; red – positive contrast; green – positive and negative contrast.

8. References

Abdul-Rahman, H.S., Gdeisat, M.A., Burton, D.R., Lalor, M.J., Lilley, F., Moore, C.J., 2007. Fast and robust three-dimensional best path phase unwrapping algorithm. Applied Optics 46, 6623-6635.

Arja, S.K., Feng, Z.M., Chen, Z.K., Caprihan, A., Kiehl, K.A., Adali, T., Calhoun, V.D., 2010. Changes in fMRI magnitude data and phase data observed in block-design and event-related tasks. Neuroimage 49, 3149-3160.

Balla, D.Z., Ehses, P., Pohmann, R., Budde, J., Mirkes, C., Shajan, G., Bowtell, R., Scheffler, K., 2013a. Functional QSM at 9.4T with single echo gradient-echo and EPI acquisition. 2nd International Workshop on MRI Phase Contrast & Quantitative Susceptibility Mapping (QSM) Ithaca, NY, USA.

Balla, D.Z., Sanchez-Panchuelo, R.M., Wharton, S., Hagberg, G.E., Scheffler, K., Francis, S., Bowtell, R., 2013b. Experimental investigation of the relation between gradient echo BOLD fMRI contrast and underlying susceptibility changes at 7T. 21st Annual Meeting and Exhibition of the International Society for Magnetic Resonance in Medicine (ISMRM 2013), ISMRM, Salt Lake City, USA, p. 300.

Balla, D.Z., Sanchez-Panchuelo, R.M., Wharton, S., Hagberg, G.E., Scheffler, K., Francis, S., Bowtell, R.W., 2012. Functional Quantitative Susceptibility Mapping (fQSM). 20th Annual Meeting and

Exhibition of the International Society for Magnetic Resonance in Medicine (ISMRM 2012), ISMRM, Melbourne, Australia, p. 325.

Beckmann, C.F., Smith, S.M., 2004. Probabilistic independent component analysis for functional magnetic resonance imaging. Medical Imaging, IEEE Transactions on 23, 137-152.

Bianciardi, M., Van Gelderen, P., Duyn, J.H., 2011. BOLD frequency shifts in human fMRI at 7T. Ultra-high field systems & applications: 7T & beyond: progress, pitfalls & potential, Lake Louise, Alberta, Canada.

Bianciardi, M., Van Gelderen, P., Duyn, J.H., 2012. Estimation of functional changes in blood oxygenation level in large veins from BOLD frequency shift and susceptibility maps. 20th Annual Meeting and Exhibition of the International Society for Magnetic Resonance in Medicine (ISMRM 2012), Melbourne, Australia.

Bianciardi, M., van Gelderen, P., Duyn, J.H., 2013. Investigation of BOLD fMRI resonance frequency shifts and quantitative susceptibility changes at 7 T. Human Brain Mapping.

Bilgic, B., Fan, A.P., Polimeni, J.R., Cauley, S.F., Bianciardi, M., Adalsteinsson, E., Wald, L.L., Setsompop, K., 2013. Fast quantitative susceptibility mapping with L1-regularization and automatic parameter selection. Magnetic Resonance in Medicine.

Chen, Z., Liu, J., Calhoun, V.D., 2013. Susceptibility-based functional brain mapping by 3D deconvolution of an MR-phase activation map. Journal of Neuroscience Methods 216, 33-42.

de Rochefort, L., Brown, R., Prince, M.R., Wang, Y., 2008. Quantitative MR susceptibility mapping using piece-wise constant regularized inversion of the magnetic field. Magnetic Resonance in Medicine 60, 1003-1009.

de Rochefort, L., Liu, T., Kressler, B., Liu, J., Spincemaille, P., Lebon, V., Wu, J.L., Wang, Y., 2010. Quantitative Susceptibility Map Reconstruction from MR Phase Data Using Bayesian Regularization: Validation and Application to Brain Imaging. Magnetic Resonance in Medicine 63, 194-206.

Deistung, A., Rauscher, A., Sedlacik, J., Stadler, J., Witoszynskyj, S., Reichenbach, J.R., 2008. Susceptibility weighted imaging at ultra high magnetic field strengths: Theoretical considerations and experimental results. Magnetic Resonance in Medicine 60, 1155-1168.

Fan, A.P., Bilgic, B., Gagnon, L., Witzel, T., Bhat, H., Rosen, B.R., Adalsteinsson, E., 2013. Quantitative oxygenation venography from MRI phase. Magnetic Resonance in Medicine.

Feinberg, D.A., Hoenninger, J.C., Crooks, L.E., Kaufman, L., Watts, J.C., Arakawa, M., 1985. INNER VOLUME MR IMAGING - TECHNICAL CONCEPTS AND THEIR APPLICATION. Radiology 156, 743-747.

Feng, Z.M., Caprihan, A., Blagoev, K.B., Calhoun, V.D., 2009. Biophysical modeling of phase changes in BOLD fMRI. Neuroimage 47, 540-548.

Glover, G.H., Li, T.Q., Ress, D., 2000. Image-based method for retrospective correction of physiological motion effects in fMRI: RETROICOR. Magnetic Resonance in Medicine 44, 162-167.

Haacke, E.M., Lai, S., Reichenbach, J.R., Kuppusamy, K., Hoogenraad, F.G.C., Takeichi, H., Lin, W.L., 1997. In vivo measurement of blood oxygen saturation using magnetic resonance imaging: A direct validation of the blood oxygen level-dependent concept in functional brain imaging. Human Brain Mapping 5, 341-346.

Haacke, E.M., Lai, S., Yablonskiy, D.A., Lin, W.L., 1995. IN-VIVO VALIDATION OF THE BOLD MECHANISM - A REVIEW OF SIGNAL CHANGES IN GRADIENT-ECHO FUNCTIONAL MRI IN THE PRESENCE OF FLOW. International Journal of Imaging Systems and Technology 6, 153-163.

Haacke, E.M., Xu, Y., Cheng, Y.-C.N., Reichenbach, J.R., 2004. Susceptibility weighted imaging (SWI). Magnetic Resonance in Medicine 52, 612-618.

Hagberg, G.E., Bianciardi, M., Brainovich, V., Cassara, A.M., Maraviglia, B., 2008. The effect of physiological noise in phase functional magnetic resonance imaging: from blood oxygen level-dependent effects to direct detection of neuronal currents. Magnetic Resonance Imaging 26, 1026-1040.

Hagberg, G.E., Bianciardi, M., Brainovich, V., Cassara, A.M., Maraviglia, B., 2012. Phase stability in fMRI time series: Effect of noise regression, off-resonance correction and spatial filtering techniques. Neuroimage 59, 3748-3761.

Hahn, A.D., Nencka, A.S., Rowe, D.B., 2009. Improving robustness and reliability of phase-sensitive fMRI analysis using temporal off-resonance alignment of single-echo timeseries (TOAST). Neuroimage 44, 742-752.

Hoogenraad, F.G.C., Reichenbach, J.R., Haacke, E.M., Lai, S., Kuppusamy, K., Sprenger, M., 1998. In vivo measurement of changes in venous blood-oxygenation with high resolution functional MRI at 0.95 Tesla by measuring changes in susceptibility and velocity. Magnetic Resonance in Medicine 39, 97-107.

Jenkinson, M., 2003. Fast, automated, N-dimensional phase-unwrapping algorithm. Magnetic Resonance in Medicine 49, 193-197.

Jenkinson, M., Bannister, P., Brady, M., Smith, S., 2002. Improved optimization for the robust and accurate linear registration and motion correction of brain images. Neuroimage 17, 825-841.

Kim, S.-G., Ogawa, S., 2012. Biophysical and physiological origins of blood oxygenation level-dependent fMRI signals. Journal of Cerebral Blood Flow & Metabolism 32, 1188-1206.

Li, L., Leigh, J.S., 2004. Quantifying arbitrary magnetic susceptibility distributions with MR. Magnetic Resonance in Medicine 51, 1077-1082.

Li, W., Avram, A.V., Wu, B., Xiao, X., Liu, C., 2014. Integrated Laplacian-based phase unwrapping and background phase removal for quantitative susceptibility mapping. NMR in Biomedicine 27, 219-227.

Liu, T., Spincemaille, P., de Rochefort, L., Kressler, B., Wang, Y., 2009. Calculation of Susceptibility Through Multiple Orientation Sampling (COSMOS): A Method for Conditioning the Inverse Problem From Measured Magnetic Field Map to Susceptibility Source Image in MRI. Magnetic Resonance in Medicine 61, 196-204.

Logothetis, N.K., 2008. What we can do and what we cannot do with fMRI. Nature 453, 869-878.

Menon, R.S., 2002. Postacquisition suppression of large-vessel BOLD signals in high-resolution fMRI. Magnetic Resonance in Medicine 47, 1-9.

Noll, D.C., Nishimura, D.G., Macovski, A., 1991. Homodyne detection in magnetic resonance imaging. Ieee Transactions on Medical Imaging 10, 154-163.

Petridou, N., Schafer, A., Gowland, P., Bowtell, R., 2009. Phase vs. magnitude information in functional magnetic resonance imaging time series: toward understanding the noise. Magnetic Resonance Imaging 27, 1046-1057.

Pfeuffer, J., van de Moortele, P.-F., Yacoub, E., Shmuel, A., Adriany, G., Andersen, P., Merkle, H., Garwood, M., Ugurbil, K., Hu, X., 2002a. Zoomed Functional Imaging in the Human Brain at 7 Tesla with Simultaneous High Spatial and High Temporal Resolution. Neuroimage 17, 272-286.

Pfeuffer, J., Van de Moortele, P.F., Ugurbil, K., Hu, X.P., Glover, G.H., 2002b. Correction of physiologically induced global off resonance effects in dynamic echo-planar and spiral functional imaging. Magnetic Resonance in Medicine 47, 344-353.

Poole, M., Bowtell, R., 2008. Volume parcellation for improved dynamic shimming. Magnetic Resonance Materials in Physics, Biology and Medicine 21, 31-40.

Rowe, D.B., 2005. Modeling both the magnitude and phase of complex-valued fMRI data. Neuroimage 25, 1310-1324.

Rowe, D.B., Logan, B.R., 2004. A complex way to compute fMRI activation. Neuroimage 23, 1078-1092.

Rowe, D.B., Meller, C.P., Hoffmann, R.G., 2007. Characterizing phase-only fMRI data with an angular regression model. Journal of Neuroscience Methods 161, 331-341.

Sanchez-Panchuelo, R.M., Francis, S., Bowtell, R., Schluppeck, D., 2010. Mapping Human Somatosensory Cortex in Individual Subjects With 7T Functional MRI. Journal of Neurophysiology 103, 2544-2556.

Schweser, F., Deistung, A., Lehr, B.W., Reichenbach, J.R., 2011. Quantitative imaging of intrinsic magnetic tissue properties using MRI signal phase: An approach to in vivo brain iron metabolism? Neuroimage 54, 2789-2807.

Schweser, F., Deistung, A., Sommer, K., Reichenbach, J.R., 2012a. Toward online reconstruction of quantitative susceptibility maps: Superfast dipole inversion. Magnetic Resonance in Medicine 69, 1581-1593.

Schweser, F., Sommer, K., Deistung, A., Reichenbach, J.R., 2012b. Quantitative susceptibility mapping for investigating subtle susceptibility variations in the human brain. Neuroimage 62, 2083-2100.

Shmueli, K., de Zwart, J.A., van Gelderen, P., Li, T.Q., Dodd, S.J., Duyn, J.H., 2009. Magnetic Susceptibility Mapping of Brain Tissue In Vivo Using MRI Phase Data. Magnetic Resonance in Medicine 62, 1510-1522.

Smith, S.M., 2002. Fast robust automated brain extraction. Human Brain Mapping 17, 143-155.

Sun, H., Wilman, A.H., 2013. Background field removal using spherical mean value filtering and Tikhonov regularization. Magnetic Resonance in Medicine.

Tomasi, D.G., Caparelli, E.C., 2007. Macrovascular contribution in activation patterns of working memory. Journal of Cerebral Blood Flow and Metabolism 27, 33-42.

Turner, R., 2002. How much cortex can a vein drain? Downstream dilution of activation-related cerebral blood oxygenation changes. Neuroimage 16, 1062-1067.

Uğurbil, K., 2012. The road to functional imaging and ultrahigh fields. Neuroimage 62, 726-735.

Weisskoff, R.M., Kiihne, S., 1992. MRI SUSCEPTOMETRY - IMAGE-BASED MEASUREMENT OF ABSOLUTE SUSCEPTIBILITY OF MR CONTRAST AGENTS AND HUMAN BLOOD. Magnetic Resonance in Medicine 24, 375-383.

Wharton, S., Bowtell, R., 2010. Whole-brain susceptibility mapping at high field: A comparison of multiple- and single-orientation methods. Neuroimage 53, 515-525.

Wharton, S., Schafer, A., Bowtell, R., 2010. Susceptibility Mapping in the Human Brain Using Threshold-Based k-Space Division. Magnetic Resonance in Medicine 63, 1292-1304.

Woolrich, M.W., Ripley, B.D., Brady, M., Smith, S.M., 2001. Temporal Autocorrelation in Univariate Linear Modeling of FMRI Data. Neuroimage 14, 1370-1386.

Wu, B., Li, W., Guidon, A., Liu, C., 2012. Whole brain susceptibility mapping using compressed sensing. Magnetic Resonance in Medicine 67, 137-147.

Zhao, F.Q., Jin, T., Wang, P., Hu, X.P., Kim, S.G., 2007. Sources of phase changes in BOLD and CBV-weighted fMR1. Magnetic Resonance in Medicine 57, 520-527.

8. Table

Table 1

Dataset	N_{fMRI}	N_{fQSM}	CC
MO_{motor1}	640	160	-0.86
MO_{motor2}	640	160	-0.86
MO_{motor3}	640	160	-0.83
MO_{motor4}	640	160	-0.86
SO_{motor1}	80	80	-0.66
SO_{motor2}	160	160	-0.79
SO_{motor3}	160	160	-0.77
$SO_{visual1}$	128	128	-0.82
$SO_{visual2}$	128	128	-0.76
$SO_{visual3}$	128	128	-0.80
$SO_{somatos.1}$	320	320	-0.80
$SO_{somatos.2}$	320	320	-0.83
$SO_{somatos.3}$	320	320	-0.82
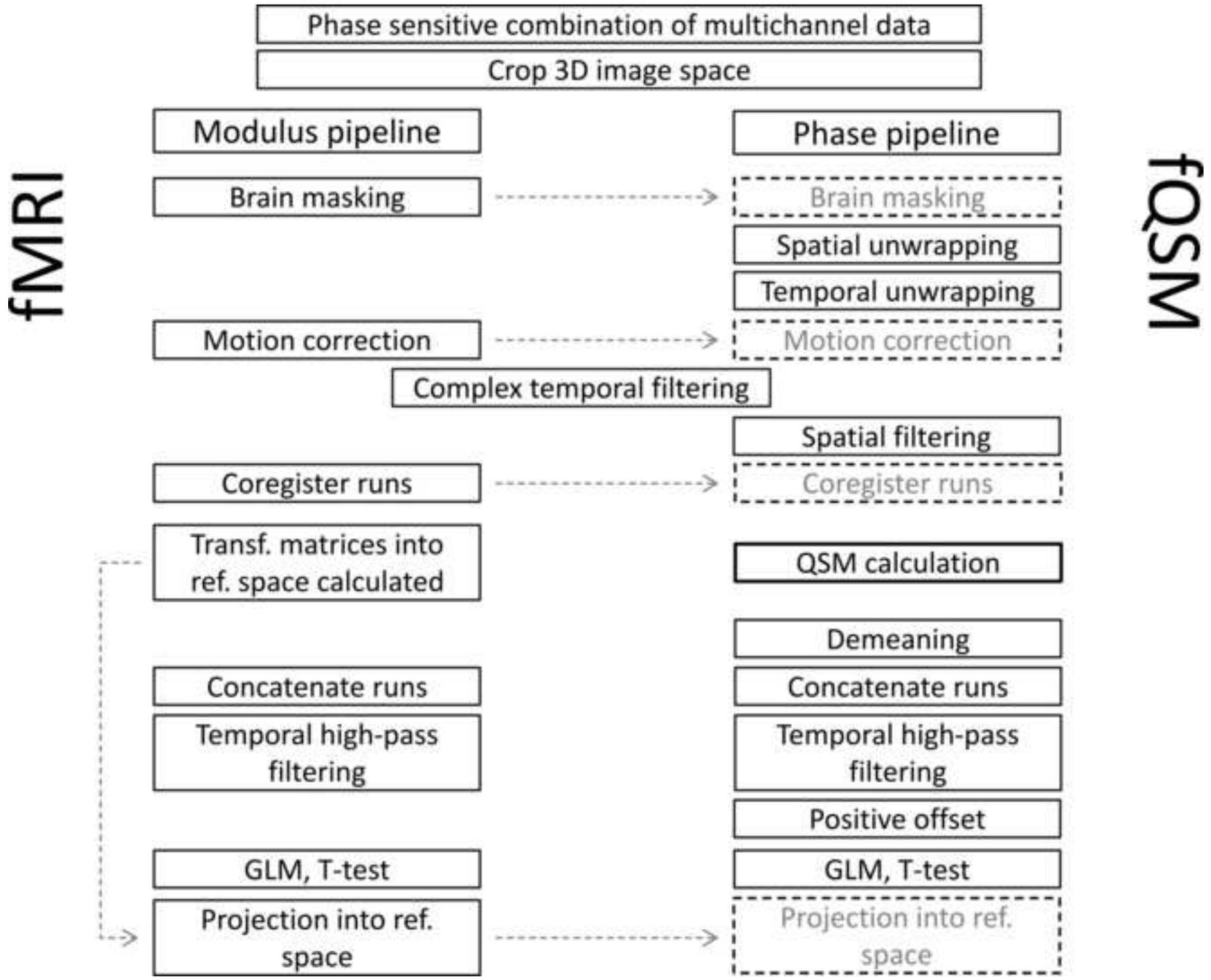
(a) coronal · (b) sagittal — 6 slices = 0.5 s acquisition

(c) transverse · $\Delta\phi_B(\angle_1)$ · (d) $\Delta\phi_B(\angle_2)$ · (e) $\Delta\phi_B(\angle_3)$ · (f) $\Delta\phi_B(\angle_4)$

0.1 / -0.1 [rad]

(a)

(b)

(c)

(d)

10. Supplementary Material

Click here to download 10. Supplementary Material: Supplementary Material_revised_140519.pdf

10. Supplementary Material